Supporting Online Material for
Translocation of Single-Stranded DNA through Single-Walled Carbon Nanotubes

Haitao Liu*,[1], Jin He*,[2], Jinyao Tang[1], Hao Liu[2,3], Pei Pang[2,4], Di Cao[2,4], Predrag Kristic[5], Sony Joseph[5], Stuart Lindsay[2,3,4,†] and Colin Nuckolls[1,†]

[1] *Department of Chemistry, Columbia University, New York, NY 10027*

[2] *Biodesign Institute,* [3] *Department of Chemistry and Biochemistry,* [4] *Department of Physics, Arizona State University, Tempe, AZ 85287.*

[5] *Physics Division, Oak Ridge National Laboratory, Oak Ridge, Tennessee 37831*

1. Fabrication of devices
2. Measurements on multiwalled tubes
3. Plasma etching and device leakage
4. Blocking of tubes by chemical modification
5. AFM diameter measurements
6. Raman measurements
7. Measurement of electrical properties
8. Measurement of electrochemical current
9. Theoretical modeling and simulation
10. pH dependence of current.
11. DNA sequences and primers
12. Translocation data for the 120 nt oligomer and spike widths
13. Quantitative Polymerase Chain Reaction

1. Fabrication of Devices:

Cobalt catalyst particles were synthesized using a block copolymer method (*1*). In brief, 0.05 g of PS-P4VP di-block copolymer (Mn-PS-b-4VP: 10400-b-19200; PDI: 1.27, Polymer Source, Inc.) was added into 12.5 ml toluene and stirred at 70^{O}C for 4–5 hours. Subsequently, 1.1 mg of $(CH_3CO_2)_2Co$ powder was added to the block copolymer solution and stirred for 24 hours at 30^{O}C. The catalyst solution was brushed onto the edge of an oxidized (300 nm SiO_2) silicon wafer. The polymer was burnt off using an oxygen plasma (Harrick Plasma cleaner, 600mTorr, 29.6W, 20 mins). The silicon wafer was placed into a thermal CVD furnace in a reducing environment of Argon and hydrogen (300 sccm and 110 sccm, respectively) and heated from 504 to 900 ^{O}C in 22 minutes, resulting in the reduction of cobalt oxide to cobalt nanoparticles. Individual SWCNTs of low defect density (Figure S1 A) were grown by a chemical vapor deposition (CVD) process from cobalt catalyst particles using ethanol as the carbon source (*2*). After growth, chips were examined using SEM in order to select those with long SWCNTs. These were immediately covered with a layer of PMMA resist (PMMA A8 or PMMA/MMA). Alignment markers were

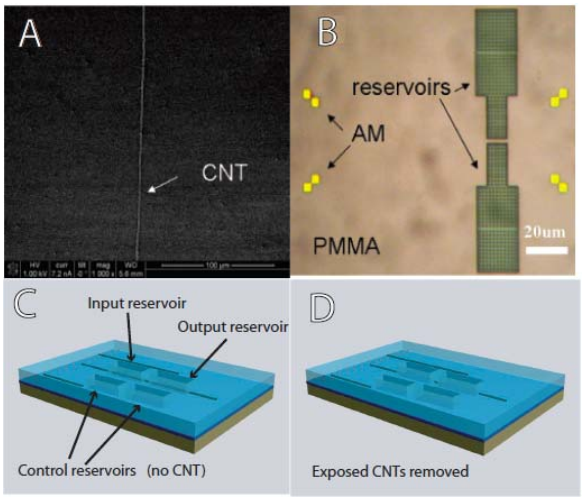

Figure S1. A) SEM image of SWCNTs as produced. B) Optical image of a device ("AM" = alignment markers). C) Layout of reservoirs etched by EBL. D) Final devise after plasma etch of exposed SWCNTs.

then created by standard electron beam lithography (EBL) procedures. The locations of SWCNTs relative to the gold alignment markers were recorded with a further round of SEM images. A second EBL process generated reservoir patterns on a 750nm layer of PMMA resist (MicroChem Co., 950 PMMA C5, baked for 2 minutes at 180 ^{O}C after spin-coating). Before measurement, the devices were developed in PMMA developer (MIBK: IPA=1:3) for 90 seconds and rinsed in IPA for 30 seconds. An optical image of a typical reservoir is shown in Figure S1 B. After drying with nitrogen, the chips were exposed to oxygen plasma (Harrick Plasma cleaner, 600mTorr, 7.3W) from 15 to 35 seconds to open the two ends of SWCNTs. The data shown in Figure 2 of the main text were obtained with etching times that were a maximum of 22s (see Fig. S5). The oxidative removal of the exposed CNT is illustrated in Figure S2 which shows an SEM image taken through a residual layer of PMMA resist (the figure also demonstrates the placement of an electrode under the barrier – see section 8). Clearly, the SWCNT under the resist remained intact.

In order to provide a fluidic pathway into and out of the reservoirs, we built a PDMS microfluidic system with embedded channels (formed by binding two layers together) to avoid leakage caused by PDMS deformation. The top PDMS layer was prepared by casting PDMS (SYLGARD 184 Silicone, Dow Corning) on a 50 μm deep SU-8 mold formed by optical lithography. The bottom PDMS layer was prepared using a mold made by deep RIE of a silicon wafer. Both parts were cured for 48 hours at room temperature. Interconnecting holes were punched through the cured PDMS using specially-formed hypodermic needles. The top and bottom PDMS layers were treated in an oxygen plasma (Harrick Plasma cleaner, 600mTorr, 29.6W) for 40 seconds to activate the surfaces. After alignment, the two layers were brought into contact and baked on a hotplate at 65℃ for 1 minute to complete the bonding process.

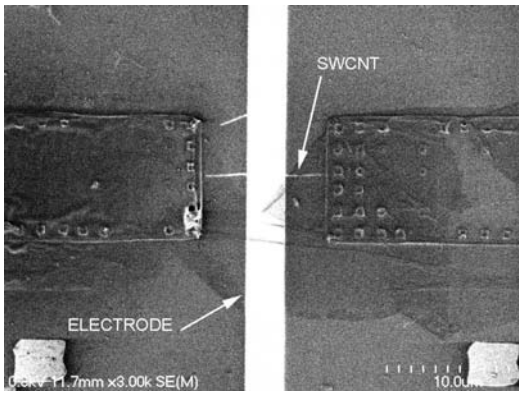

Figure S2: SEM of a device taken after oxygen plasma treatment followed by removal of most of the PMMA layer to enable visualization of the SWCNT under the barrier. This image also shows an electrode used to contact the SWCNT under the barrier.

The PDMS microfluidic fluidic system formed a good seal with the freshly oxygen-plasma-treated PMMA layer on the devices and the reservoirs wetted readily on injection of fluid into the system.

2. Measurements using multiwalled tubes

MWCNTs were purchased from Sigma-Aldrich inc. with stated outer diameters between 10-30nm and stated inner diameters between 5-10nm. The nanotubes were dispersed in PMMA A5/DMF (1:1, *v*/*v*) using mild stirring for 24 hours for a final concentration of about 0.1mg/ml. The nanotube/PMMA/DMF mixture was brushed onto the surface of a silicon wafer and the substrate was baked at 180 ℃ for 10min and then transferred into a tube furnace immediately for PMMA removal. PMMA was removed by heating the substrate to 400 ℃ under 300 sccm Ar flow for at least 1 hour. An AFM image of an MWCNT after PMMA removal is shown in Figure S3a.

The chips were completed as described above for the SWCNT devices. The yield of opened tubes after oxygen plasma treatment was extremely low, giving only two working devices out of a total of 30 that were made. Translocation of the 60 nt oligomer through one of these devices (0.1 nM in 2 M KCl) was marked by the fast current dips characteristic of current blockades in larger nanochannels at high salt. (*3*) Data are shown in Figure 3b. PCR analysis of fluid collected from the output reservoir (Figure S3c) confirmed that these spikes signaled translocation of the DNA oligomer.

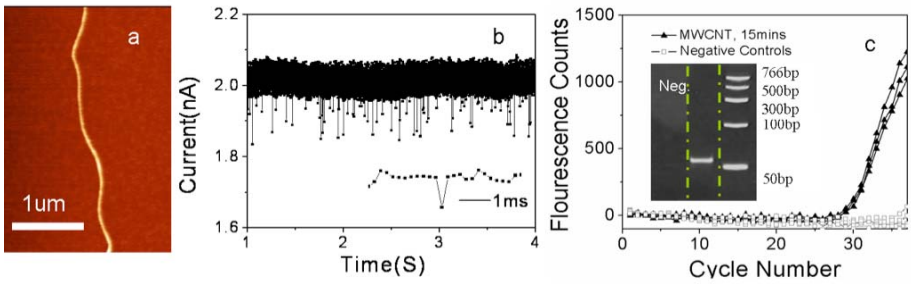

Figure S3 a) An AFM image of a MWCNT. b) Typical signal of 1nM 60nt ssDNA in 2M KCl translocation through MWCNT device at bias 0.2V. The inset shows an expanded current dip with a width of about 0.2ms. A distribution is shown in Fig. S14. c) Results of q-PCR and gel analysis of the ssDNA collected in the outlet reservoir (a control sample produced a negative PCR result).

3. Plasma etching and device leakage

There are three possible leakage paths for the measurements as illustrated in Figure S4 A-C. The first one is between the oxidized silicon substrate or the CNT exterior wall and the PMMA layer. The second one is between the PMMA layer and the PDMS surface. The third one is between the exterior walls of CNT bundles. We rigorously tested all the possibilities and the results are summarized in Figure S4 and Figure 1C of the main text. No ionic current was detected for all the measured devices (total 31) before using the oxygen plasma (Harrick Plasma cleaner, 550-600mTorr, 7.2W, 22 seconds) to open both ends of the bridging CNTs. This control experiment shows that leakage path 1 is unlikely. Leakage path 2 was found in some measurements. To avoid such leakage, control devices, lacking bridging CNTs in the barrier, were fabricated along with functional devices on the same chip. Control devices are always measured before and in between real device measurements. Occasional leakage due to contamination can be eliminated by cleaning both PMMA and PDMS surfaces or using a new PDMS cover. Leakage created by oxygen plasma damage of the PMMA surface was carefully monitored. As shown in Figure S5, no measurable current is found in the control devices if oxygen plasma treatment is limited to a maximum of 22s. For the fraction of devices shown by SEM to be unopened by this plasma etch,

we found no measurable current (Figure S4F). This result provides additional evidence that no new leakage path (path 1 or 2) appears after routine oxygen plasma treatment. Leakage along path 3 is possible, but as SWCNT's are the main product in our growth conditions it is unlikely.

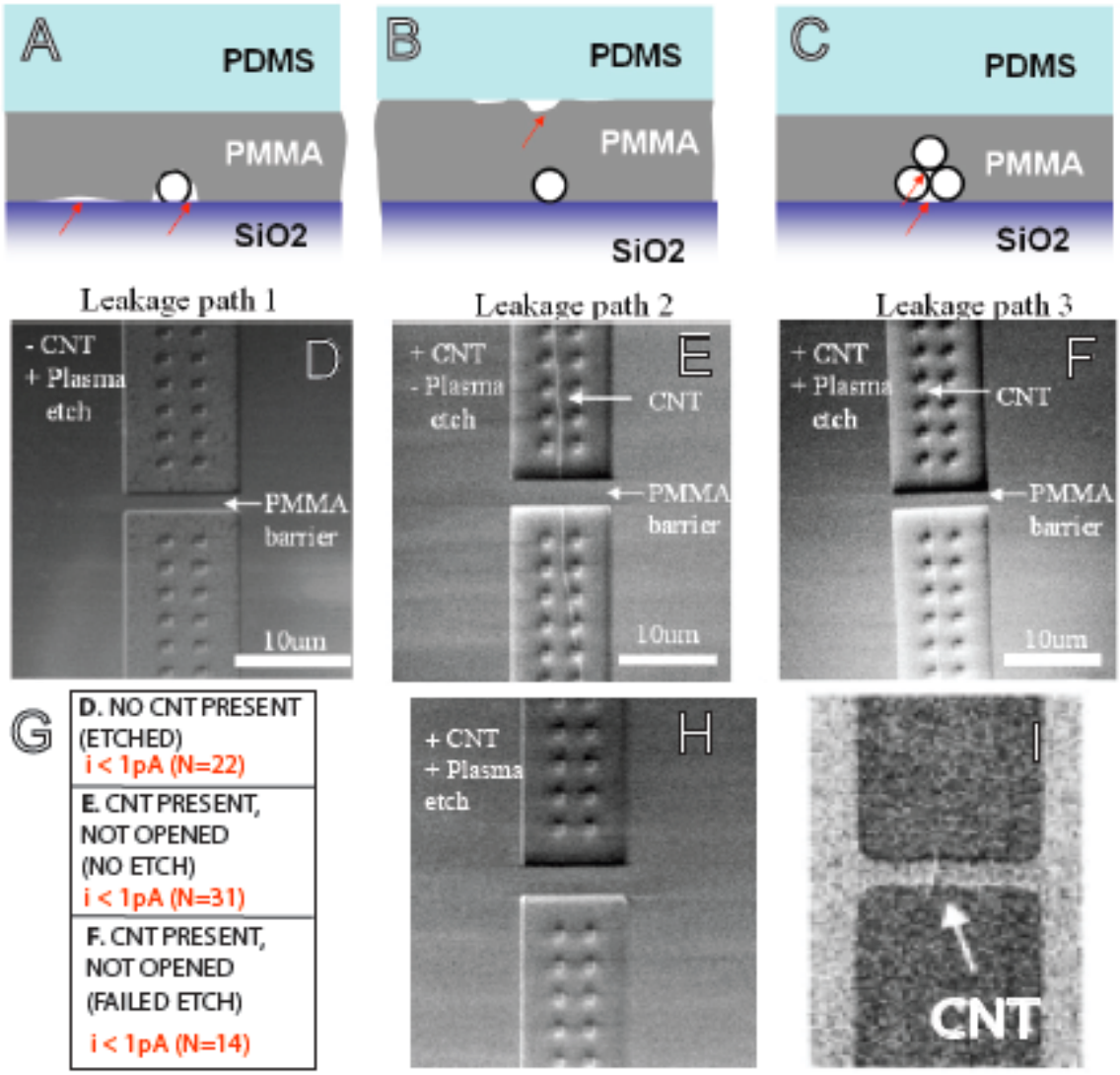

Figure S4: (A-C) Three possible leakage paths are illustrated. The red arrows point to the possible leakage path locations. The black circles represent a cross section through a SWCNT. (D) SEM image of a device lacking a SWCNT. (E) SEM image of a device with a CNT crossing the fluid barrier, but unopened by a plasma etch. (F) SEM image of a device with a CNT crossing the barrier and subject to a plasma etch with the SWCNT remaining unopened. (G) Summary of the measured leakage currents for the control devices described in D-F. (H) SEM image of a device in which the exposed SWCNT was removed by plasma etching. The current distribution for these opened devices is shown in Figure 1C of the main text. (I) SEM image of a device like that in H with the PMMA layer removed to show the remaining SWCNT under the barrier.

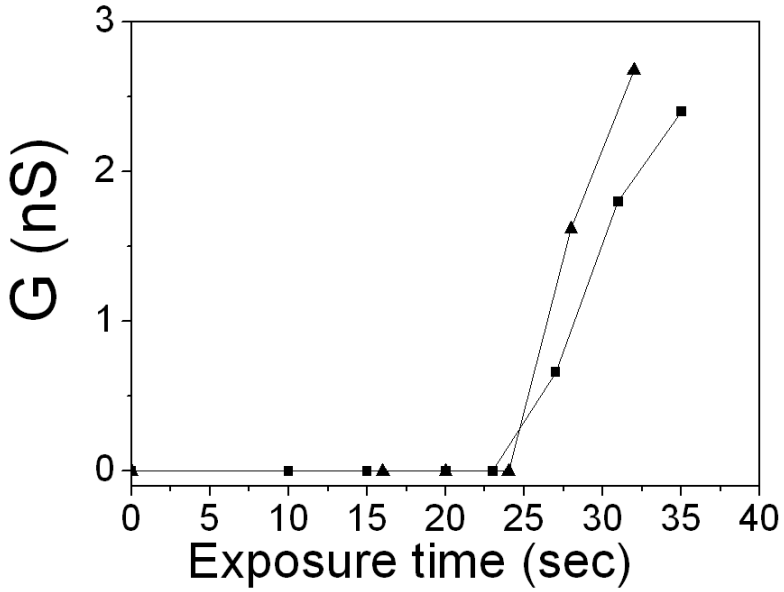

Figure S5: Conductance owing to leakage of two control chips (2 μm gap) versus oxygen plasma exposure time. The oxygen plasma is 7.2W at about 550mTorr.

4. Blocking of tubes by chemical modification

The nanofluidic device was treated with O_2 plasma to open the tube. Both reservoirs of the devices were filled with pure water and then replaced with an aqueous solution of KCl (1 M) and phosphate buffer (20 mM, pH = 7). Two Ag/AgCl electrodes were used to measure the ionic current through the CNT. To modify the ends of the CNT, we used the well established EDC/sufo-NHS chemistry to activate the terminal carboxylic acid groups of the CNT ends and couple them to amine functionalized polyethylene glycol (PEG) (*4, 5*). Briefly, one of the reservoirs was flushed and filled with a solution of EDC (0.1 M) and sulfo-NHS (20 mM). The solution was left in the reservoir for 3 hrs. The reservoir was then flushed and refilled with a solution of methoxypolyethylene glycol amine (Fluka, MW: 750, 20 mM) and allowed to react for 20 min. The reservoir was then flushed and refilled with the KCl-phosphate buffer solution and the ionic current was measured again.

After the chemical modification, the ionic current became asymmetric; the current being higher if the modified channel is *negatively* biased relative to the pristine channel than if the modified channel is *positively* biased relative to the pristine channel. The result shown in Figure S6 refers to the lower current value. The current became nearly symmetrical after both channels were modified.

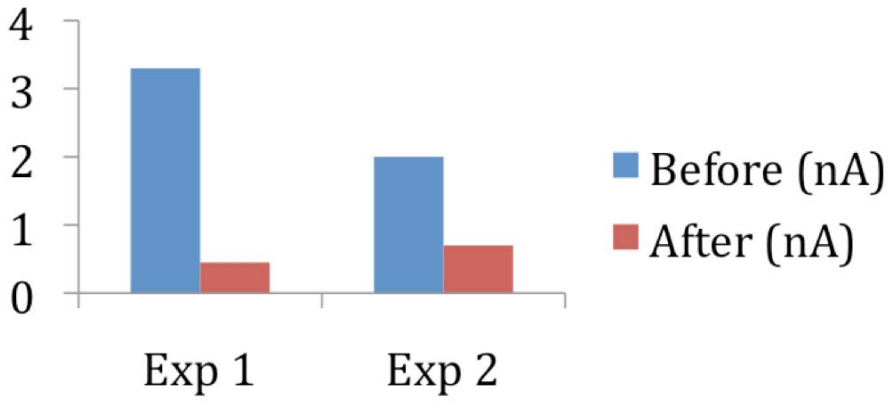

Figure S6: Effect of covalent modification on the ionic current (bias: 0.300 V).

5. AFM diameter measurement

We first measured the diameter of as-grown CNTs using the height determined in AFM tapping mode images. A typical image and a height distribution determined from many images are shown in Figures S7a and S7b. To measure the height of the particular tubes used in ion current and DNA translocation measurements, the PMMA reservoir material was stripped off using CH_2Cl_2 and the surface further cleaned by heating at 400 ^{o}C in an Ar flow for at least one hour. An example of an AFM measurement on a recovered tube is shown in Figure S7c. We chose areas that appeared to be clean to make measurements, but repeated measurements varied significantly (error bars in Figure 2C of the main text) likely as a consequence of local contamination.

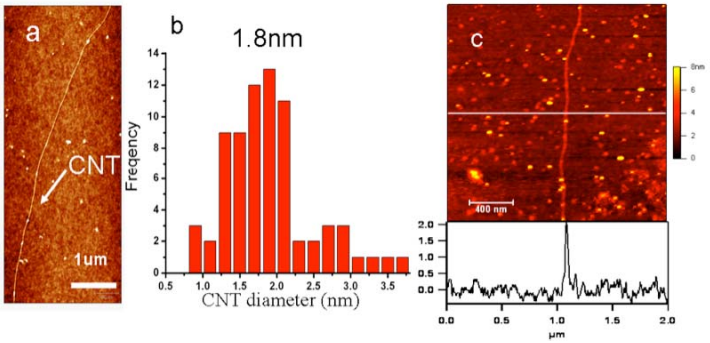

Figure S7. a) An AFM image of SWCNT after growth. b) A typical distribution of CNT diameters measured by AFM. The modal diameter is 1.8nm and tubes up to 9 nm diameter have been found. c) An AFM of a SWCNT after ionic current measurement taken after stripping of the PMMA barrier.

6. Raman measurements

A micro-Raman system (Renishaw inVia Raman microscope) was used with excitation at 632.8nm (1.96eV). The laser beam was focused down to a 4 μm spot with a power of 17 mw using a 50x microscope objective. Typical spectra are shown in Figure S8. The diameter of CNT is normally determined from the radial breathing mode (RBM) but the RBM peak was too weak for most of the CNTs measured. We used the two G bands instead with $\omega_G^- = \omega_G^+ - C/d_t^2$, where C=79.5 cm^{-1} for metallic tubes and 47.7cm^{-1} for semiconducting tubes (*6*). The G band line

shapes also indicate the electrical properties of the tubes (*7*) and this was found to be consistent with the electrical measurements made on CNT FETs. The D mode peak was weak in pristine CNTs but became strong after the treatment used to remove PMMA layer.

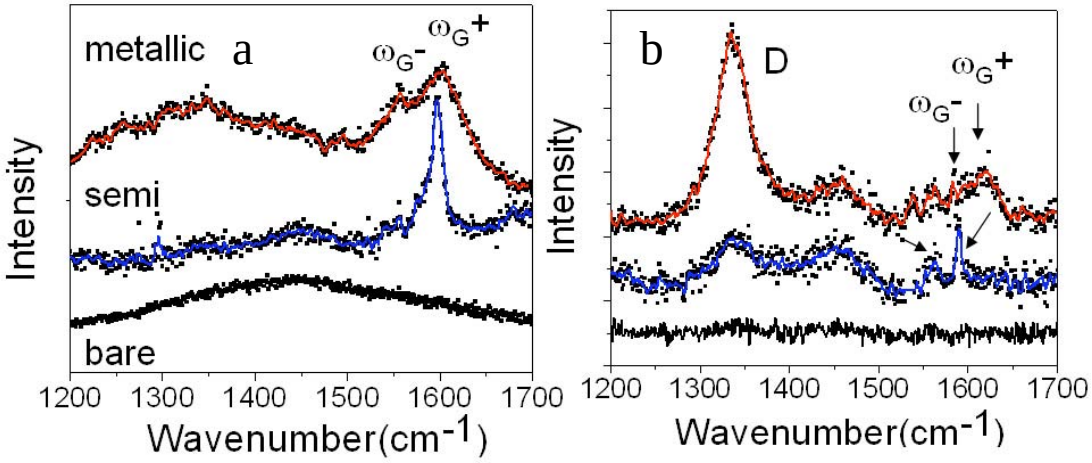

Figure S8. Raman spectra of a) pristine CNTs and b) CNTs after treatment to remove the covering PMMA layer. We show spectra for both a metallic (red) and a semiconducting (blue) tube. The black dots are raw data and the solid lines are obtained after smoothing. Raman spectra of SiO_2 substrate alone are shown at the bottom (black).

7. Measurement of electrical properties

We fabricated field effect transistor (FET) devices to characterize the electrical properties of the CNTs that were used in the mass transport studies. After the measurement of the ionic current and testing for DNA translocation, the wafer was soaked in CH_2Cl_2 solution overnight to remove the PMMA layer that was used to fabricate the nanofluidic devices. A new PMMA film was then spin coated onto the wafer (MicroChem PMMA A5, 3000 rpm) and baked at 180°C for 2 min. Electrical contact to the CNT was patterned by e-beam lithography and developed with 3 : 1 MIBK : IPA developer. Gold (30 nm) was thermally evaporated onto the patterned PMMA layer with 3 nm of Cr or Ti as the adhesion buffer layer. Lift off was achieved by soaking the wafer in CH_2Cl_2 solution overnight. In some cases, the PMMA layer used to fabricate the nanofluidic device was not removed and used directly in the e-beam lithography process. Typical channel lengths of the FET device ranges from 5 μm to several tens of μm. Electrical properties of the CNT FET devices were measured with a probe station and a semiconductor parameter analyzer. Large gating hysteresis was observed; this is typical for un-passivated CNT FET devices fabricated on SiO_2. The results are summarized in Table 1 of the main test. Some typical I_{SD} vs. V_{GS} characteristics are shown below in Figures s9 and s10.

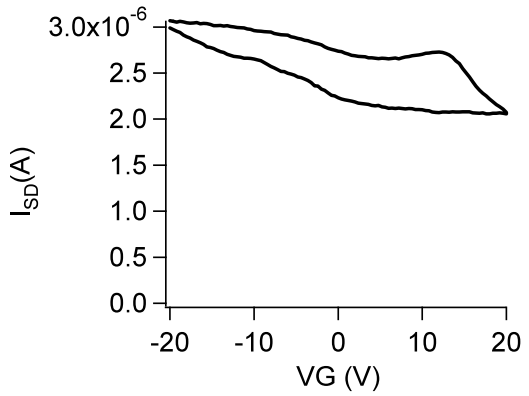

Figure S9: Typical plot of drain current vs. gate bias for a metallic tube for V_{SD}=0.50V (HL_4_1_39 Device P6).

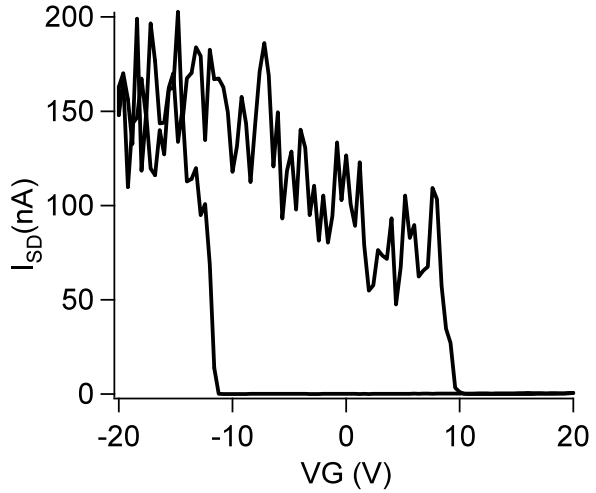

Figure S10: Typical plot of drain current vs. gate bias for a semiconducting tube for V_{SD}=0.50V (HL_4_1_37 Device AB20).

8. Measurement of electrochemical current

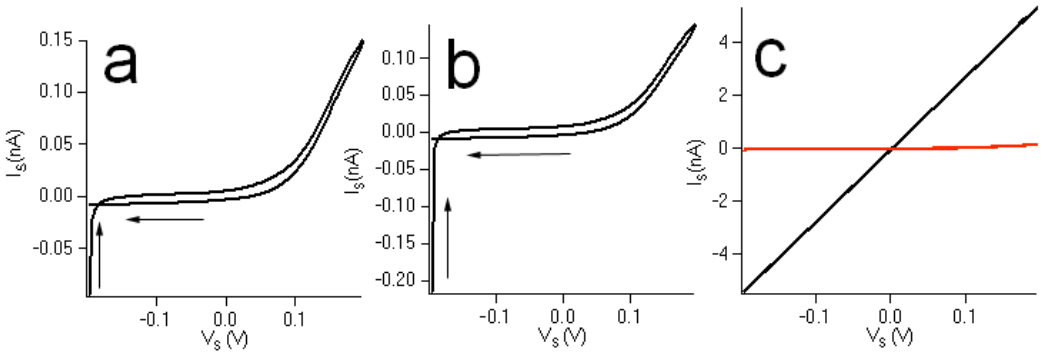

Figure S11: Electronic currents into the tube as a function for a bias V_s between the tube and an AgCl reference electrode in the input reservoir (a) and the output reservoir (b). (c) Shows both this current (red curve) and the ionic current through the tube (black curve). For the red curve, V_s is the bias between the AgCl reference electrode in one reservoir and the tube, while for the black curve, V_s is the bias applied between the reference electrodes in the input and output reservoirs.

A device was fabricated with a 3 μm wide Au electrode (30 nm Au on 3 nm Cr) contacting an SWCNT under a 10 μm wide PMMA barrier (c.f. Figure S2). The electrochemical current was measured with the tube grounded and a bias sweep between 0 and ±0.2V with respect to the Ag/AgCl electrodes (which are at a resting potential of 0.22V vs. NHE in 1M KCl). If the potential drop across the floating SWCNT is symmetrical and all concentrated at the ends of the tube, this would correspond to a total applied potential difference of 0.8V, because 0.4V would be dropped at each end of the tube in the bipolar electrode configuration. This is much higher than any of the biases used in this work (even more so if there is any significant potential drop across the tube itself). The results are summarized in Figure S11. Electrochemical current through the grounded tube is shown for current into the input reservoir in (a), and into the output reservoir in (b). For the CNT biased > -0.1V with respect to the Ag/AgCl electrode, a reduction current is observed, and the linear rise in current suggests that it is diffusion limited. The Au-Cr contact will generate a Schottky barrier (*8*) but the symmetry of the curves suggests that this is not a significant effect. The currents observed here are much higher than those reported for a CNT electrode without exposed ends, (*9*) suggesting that the electrode kinetics are enhanced at the ends of the tube.

These currents represent an upper limit to the electrochemical current because the potential drops in the bipolar configuration will be much smaller. Figure S11c shows a plot of the ionic current through the tube as a function of the potential applied between the two Ag/AgCl electrodes plotted together with the electrochemical current plotted as a function of the potential difference between the tube and one Ag/AgCl electrode. This shows that the maximum possible contribution of electrochemical current is minimal. The CNT remains stable after repeated electrochemical cycling as shown by SEM examination of the CNT after stripping the PMMA (Figure S2).

9. Theoretical modeling and simulation

Molecular dynamics (MD) simulations were performed using GROMACS 4.0.3 on the Cray-XT5 of NICS, University of Tennessee in Knoxville. For the MD simulations, different types of metallic

SWCNT are considered, shown in Table SI (the center-to-center diameters are reduced by 0.34 nm). The force field and the simulation setup are as in (*10*).

We first computed by molecular dynamics simulations the ion mobility (defined as the mean ion velocity in the direction of field divided by electric field) and diffusion coefficients (defined as a slope of mean square displacement in the axial direction vs. time). We found that these were not too different from the bulk for CNT diameter of 2 nm, with a trend of increasing with further decreases of the diameter. However these variations of the mobility and diffusion coefficients could not account for the magnitude of the measured ion currents.

The simulation is first performed with water baths of 2 nm size attached to the ends of a tube. The reservoirs were filled with water and neutral electrolyte of an average concentration c. Once equilibrium water content inside the tube was reached, such that the ends of the bath were at bulk water density, baths were removed and NVT simulations were performed for infinitely long tubes at various excess ionic volume charge densities ranging from 0.5M to 4M. We assumed that there is an excess volume density of a charge of one sign in the CNT arising likely by the "filtering" at the CNT ends. This excess charge comes on the top of concentration c of ions of both signs. For example if the bulk concentration of KCl is 1 M and the excess concentration of K^+ is 2M, then the resultant concentration of potassium ions is 3M, while the Cl^- concentration remains at 1M. For ions, the Lenard-Jones parameters are the same as in (*11*). An external electric field E_{ext}=0.002 V/nm was used to drive the ions. The electro-osmotic velocities of water are averaged in the steady state, a few ns after the simulations started. The average electro-osmotic velocities as function of a SWCNT diameter at various volume charge densities are given in Table SI, while dependence on volume charge in the SWCNT for the (10,10) tube is shown in Table SII, scaled to the experimental value of the electric field.

CNTs	**(10,10)**	**(16,16)**	**(20,20)**	**(24,24)**	**(32,32)**	**(48,48)**
External diameter (nm)	1.6960	2.5096	3.0500	3.5944	4.679	6.8488
Electro-osmotic velocity (m/s)						
Volume charge n= 2M	2.90	1.03	0.70	0.71	0.70	0.60
density n = 3M	3.63	0.92	0.59	0.66	0.45	0.36
n = 4M	4.93	1.38	0.80	0.41	0.44	0.18

Table SI. Electro-osmotic velocities as functions of the SWCNT diameter.

CNT (10,10)							
Volume charge density n(M)	0.25	0.50	1.0	1.5	2.0	2.5	3.0
Electro-osmotic velocity (m/s)	0.52	1.23	1.94	2.33	2.94	3.08	3.63

Table SII. Electro-osmotic velocities in function of the excess volume charge density in the tube.

The Poisson equation is expressed as

$$\nabla \cdot (\varepsilon_r \nabla \phi) = -\frac{\rho}{\varepsilon_0} \qquad (1)$$

where ϕ is the local electrical potential in the simulation domain, ε_0 and ε_r are the electrical permittivity of the vacuum and the relative permittivity, respectively; ρ is the volume charge density, given by

$$\rho = F\sum_{i=1}^{N} z_i c_i \tag{2}$$

F is the Faraday constant and c_i is the concentration (M) of species i.

The Nernst-Planck equation governs the transport of the ions:

$$\frac{\partial c_i}{\partial t} + \nabla \cdot J_i = 0 \tag{3}$$

and

$$J_i = -D_i \nabla c_i + \vec{v} c_i - \mu_i z_i c_i \nabla \phi \tag{4}$$

where J_i is the flux of the *i*th species, $\vec{v}$ is the velocity vector of water whose motion is dragging all ions i, μ_i and D_i are the electrophoretic mobility and diffusivity of the species, and z_i is the valence of the species.

Finally,

$$\Gamma_i = F z_i J_i = F\left(-z_i D_i \nabla c_i + \vec{v} z_i c_i + \mu_i z_i^2 c_i \left(-\nabla \phi\right)\right) \tag{5}$$

where Γ_i is the current density contributed by the *i*th ion. Integrating Γ_i over the area of cross section and summing over the different species gives the total current. The three components of the current, the diffusive, electro-osmotic and electroporetic all contribute to the ionic current. However, with the conditions of high water flow rate, induced by the slipping over the smooth hydrophobic CNT surface (10), and excess volume charge of anions or cations, the electro-osmotic term is by far the dominant contribution to the current, i.e.

$$I \approx SFnv \tag{6}$$

where S is the CNT center-to-center cross sectional surface area, n is the average volume density (the number of moles per liter of the solution) of the excess charge ions (i.e. $\sum_i z_i c_i$ averaged over the tube cross section, S), and v is the electro-osmotic velocity, averaged over S. The actual number of ions included in the system varies with the CNT diameter (i.e. with enclosed volume) because the enclosed charge is the product of n and the volume enclosed by the SWCNT. Because 2D computations for the system dimensions of the order of the experimental setup would be computationally formidable, we performed 1D Poisson-Nernst-Planck (*12*) calculations with the water velocity inside the tube as an input from the molecular dynamics simulations and flow outside the tube based on the continuity equation. The baths was taken to be 10 micrometers and the tube length 2 micrometers. For various electrophoretic fields the electro-osmotic velocities inside the tube were scaled assuming a linear dependence on the electric field. This is supported by our calculations using a weaker electrophoretic field (0.001 V/nm), which yields flows rate that vary approximately linearly with the field. However, for weaker fields the statistical noise prevents accurate determination of the flow velocities.

In order to verify the validity of the 1D approach, we performed 2D calculations with the Stokes flow approach for a drastically reduced geometry, but there was no significant difference in the flow physics.

Finally, the fact that the CNT is fixed in space, defining the system at rest, and that we have applied periodic boundary conditions for water and ions ensures we are getting the flow relative to the "infinite" tube and Newton's third law is not violated. Normally in molecular dynamics center of mass motion is removed (the default in GROMACS). Since we are using non-equilbrium molecular dynamics, we explicitly turned off the removal of the center of mass motion so that the steady state velocity v reached by water is the average electroosmotic velocity of water with respect to the fixed walls (that is akin to fully developed flow in a pipe). This velocity is then used as entry into the Nernst-Planck equations (Eq. (2) of S9) to solve for the electric current due to the mobility, diffusion and electroosmotic flow. In the steady state (as is a case in the experiment), the ions or water molecules enter the system from one end and exit at the other end without accumulation or depletion. Furthermore, the volume of the experimental baths is extremely large in comparison with the very small tube volume. For modeling purposes the baths can be considered infinite reservoirs of ions, whose concentrations do not change when ions enter or leave the baths.

For the (10,10) SWCNT, the dependence v(n) in Table SII fits a power law, $v(n) = a_1 n^{b1}$, where a_1 =1.72 and b_1 =0.74, where n is molar concentration and a_1 in m/s. However, to express v (and therefore the measured I in Eq. (6)) in terms of the KCl concentration c, we need n(c), an unknown quantity. Using the measured dependence of the system conductance G on c, Eq. (5) yields $G(c) = FSn(c)v(n(c))/V$, where V is the applied voltage (in V). A general assumption of a power law for n(c), i.e. $n(c) = a_2 c^{b_2}$, leads to a power law dependence for $G(c) = Ac^B$. From measured data, we deduce A=9.64 and B=0.39, which finally gives $n(c) = 3.31c^{0.22}$. The measured I-V characteristics of Fig. 2A for the (10,10) SWCNT are then easily obtained using n(c).

In summary, if there is an excess ion volume density in the CNT, the resulting electroosmotic flow gives rise to electric currents that are as large as the measured values. The other components of the current (electrophoretic, diffusion) depend on the bulk concentration of the electrolyte but stay much smaller than the electroosmotic contribution, independent of the bulk electrolyte concentration c. The main reason we used the fitting method above was that the excess number of ions inside the tube was not known *a priori*. Since we presently have no means to know or simulate the chemical composition and charge of the functional groups at the entrance of the SWCNTs, we cannot obtain the excess charge in the CNT except by fitting to measured values. Therefore, the power law for n(c) we presented above results from the best fit to the measured results.

The fit derived from the concentration dependence (Figs. 2A,B) also produces a consistent fit to the diameter dependence of the current (Fig. 2C) adding some plausibility to this model. The volume charge as function of the CNT diameter is also an unknown. The data in Fig. 2C was reproduced with a range of an excess volume charge in the tube from 2M to 4M, for the given KCl concentration = 1M. The MD calculation of $v^n(R)$ for various fixed n (Table SI) was used to compute $G^n(c) = FSnv^n(d)/V$. We note that the Fig. 2C contains two branches of data, for the same diameters of tube. We believe that the multivalued structure of the measured data is a consequence of variation of the excess volume charges in various tubes. The results of Figs. 2A and B correspond to the higher branch in Fig. 2C and may give a hint on the nature of the filtering mechanism which causes the excess volume charge in a tube.

10. pH dependence of current.

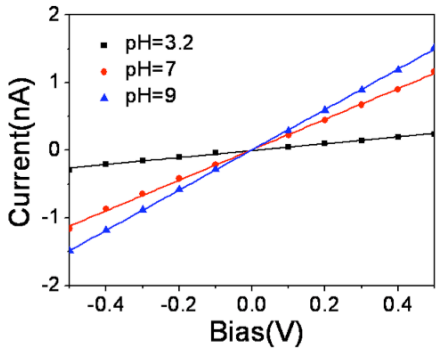

Figure S12: Typical current-voltage curves for a SWCNT as a function of the pH of 0.1M KCl with 1mM PBS. The measured conductance is 2.98 nS at pH9 (black squares), 2.25 nS at pH7 (red circles) and 0.51 nS at pH3.2 (blue triangles).

The pH of KCl solutions was adjusted by adding HCl or KOH and conductance measured for a number of tubes. A typical data set is shown in Figure S12. Reducing the pH of the KCl solution resulted in a substantial reduction of the current through the tube. This presumably reflects protonation of the carboxylic acid residues at the end of the tube (pKa ≈ 4.5 (*13*)) showing that the charge distribution at the end of the tube plays a significant role in determining the current through the tube.

11. DNA sequences and primers

We started with a random 60nt sequence with ~50% GC content, and adjusted it to minimize the secondary structure predicted by mFold (http://mfold.bioinfo.rpi.edu/cgi-bin/dna-form1.cgi) for 1M Na^+ and 23°C. The sequence used (IDT, Corvallis) was:

5' - TAC CAG AGA CCG TCA GAG CTA CGG ACA GTC CGT GTT AGG TTG GTA ATC CAA CAC GAG GTA - 3'

Primer lengths were chosen to give a melting temperatures near 60 °C:

Forward primer:

5' - CAG AGA CCG TCA GAG CTA CGG A -3' 22nt

T_M in 50mM NaCl = 60 °C

Reverse primer:

5' - TAC CTC GTG TTG GAT TAC CAA CCT A-3' 25nt

T_M in 50mM NaCL = 57.3 °C

A similar process was used to design the 120 nt oliomer and primers:

5'-GTA TCA GAT TAG TGC ACG GTA GAC TCA AGC AGA TTA CTC ACG TGA ATG TTA ATA GTT GGA CGC TCG GAT AGC CCA GTT ACT ACA AGA GCC TTA ATA CGTGCA TCA GGT GTG TAA GCA ACT-3'

Forward primer:

5’-CGGTAGACTCAAGCAGATTACTCACG-3’
T_M in 50mM NaCl = 58.6 °C

Reverse primer:

5’- AGGCTCTTGTAGTAACTGGGCTATCC-3’
T_M in 50mM NaCl = 59.5 °C

12. Translocation data for the 120 nt oligomer and spike widths

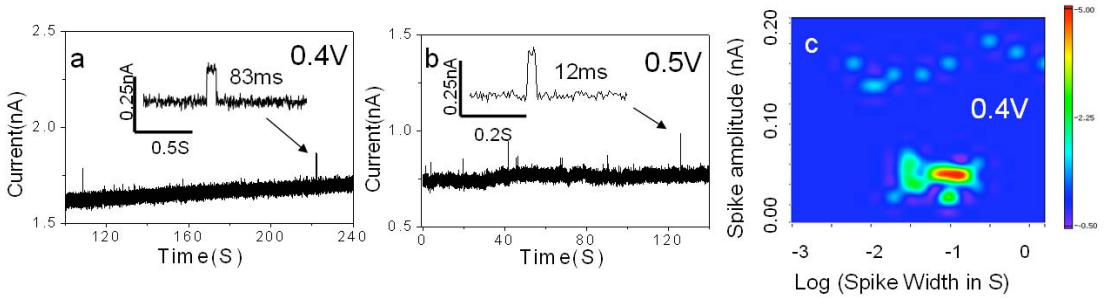

Figure S13: Representative current vs. time data at a of bias 0.4V(a) and 0.5V (b) from translocation of a 120 nt oligomer. The spike frequency is about an order of magnitude lower than for 60 nt DNA. The PCR results for this run are shown as the entry under AAnew1 in Table 1 of the main text. (c) Histogram of spike events (count is color-scaled) as a function of the log of spike duration and amplitude at a bias of 0.4V. The spike duration was around 100ms and spike amplitude varied from 50 pA to 0.2 nA.

Representative current-time traces are shown for translocation of the 120 nt oligomer in Figure S13, together with an amplitude-spike-duration distribution. The tightly clustered data around 50 pA and 100 ms reflects the small additional pulses sometimes observed at high bias (most obvious in Figure S13b). This smaller set of pulses is observed in some tubes for 60 nt translocation also. The larger spikes (amplitudes about 150 pA) are always seen on translocation, and they have significantly longer duration for this 120 nt oligomer than those observed for translocation of the 60 nt oligomer (Figure S14).

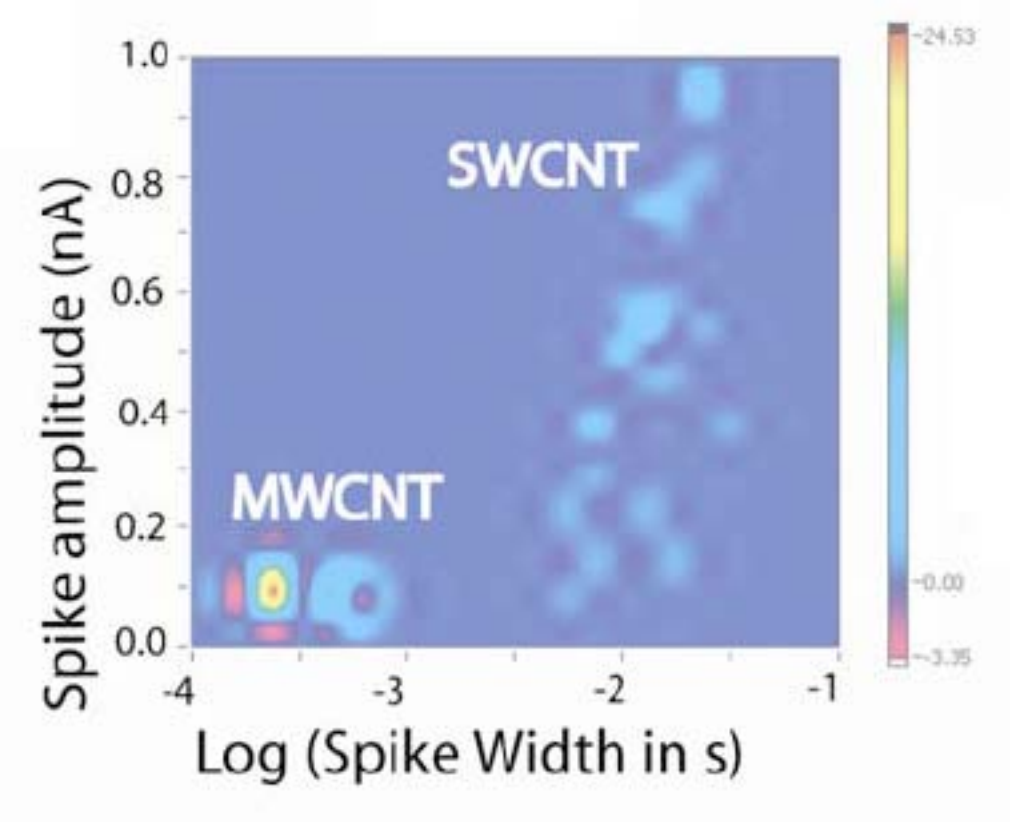

Figure S14: Histogram of spike events (count is color-scaled) as a function of the log of spike durations and amplitude. Spike duration was around 10ms and spike amplitude varied from 100 pA to 1 nA. For comparison, we also plot amplitude and duration data for negative-going current spikes (current-blockades) observed in a multiwalled tube ("MWCNT" - see Fig. S3b).

13. Quantitative Polymerase Chain Reaction

Quantification of translocated DNA is performed by quantitative real-time polymerase chain reaction (qPCR) (*14*) . We used SYBR Green® I quantification chemistry in our analysis (Bio-rad IQ SYBR Supermix® system). A standard curve was established using the Eppendorf Mastercycler® realplex system using seven 10-fold dilutions, starting with 1×10^7 template copies and ending with 10 copies. SYBR Green I quantification chemistry is sensitive to primer dimers and false priming so we verified our PCR specificity with both melting curve analysis and native 8% PAGE gel analysis to verify dsDNA product. The PCR hood, tube, pipette and pipette tips are wiped with bleach and ethanol and UV-sterilized before each run. The temperature cycles were as follows: 95°C for 5min, 92°C for 15sec, 60°C for 2sec, 72°C for 15sec for a total of 40~50 cycles. For the melting curve analysis we used 95°C for 15sec, 60°C for 15sec, and a 60°C to 95°C temperature ramp over 20 minutes.

Translocation samples were desalted using a Microcon YM-10 Centrifugal Filter. We found that the recovery was strongly dependent on the DNA concentration. The Table below plots the correction factor required (R_F is the multiplier applied to correct for losses) as a function of the number of molecules placed into the filter. At low copy number, the filter recovers only 20% of the sample.

Number of molecules	Filter recovery multiplier (R_F)
100	5
1000	2
10000	1.5
100000	1.43

Table S III: Filter recovery efficiency

References

1. B. Sreekar, R. Alfonso, Q. Jifa, K. Jing, A. M. Belcher, *Nanotechnology* **17**, 5080 (2006).
2. L. Huang, X. Cui, B. White, S. P. O'Brien, *J. Phys. Chem. B* **108**, 16451 (2004).
3. R. Fan *et al.*, *Nano Lett.* **5**, 1633 (2005).
4. N. S. DeSilva, *Am. J. Respir. Cell Mol. Biol.* **29**, 757 (2003).
5. Z. Grabarek, J. Gergely, *Anal. Biochem.* **185**, 131 (1990).
6. A. Jorio *et al.*, *Physical Review B* **65**, 155412 (2002).
7. S. D. M. Brown *et al.*, *Physical Review B* **63**, 155414 (2001).
8. Y.-F. Chen, M. S. Fuhrer, *Nano Lett.* **9**, 2158 (2006).
9. I. Heller *et al.*, *Nano Lett.* **5**, 137 (2005).
10. S. Joseph, N. R. Aluru, *Nano Lett.* **8**, 452 (2008).
11. S. Koneshan, J. C. Rasaiah, R. M. Lynden-Bell, S. H. Lee, *J. Phys. Chem. B* **102**, 4193 (1998).
12. B. T. Hughes *et al.*, *Microfluidics and Nanofluidics* **6**, 761 (2008).
13. S. Wong, E. Joselevich, A. T. Woolley, C. L. Cheung, C. M. Lieber, *Nature* **394**, 52 (1998).
14. C. A. Heid, J. Stevens, K. J. Livak, P. M. Williams, *Genome Research* **6**, 986 (1996).